Science Advances
AAAS

Supplementary Materials for

Multi-principal elemental intermetallic nanoparticles synthesized via a disorder-to-order transition

Mingjin Cui, Chunpeng Yang, Sooyeon Hwang, Menghao Yang, Sean Overa, Qi Dong, Yonggang Yao, Alexandra H. Brozena, David A. Cullen, Miaofang Chi, Thomas F. Blum, David Morris, Zou Finfrock, Xizheng Wang, Peng Zhang, Vitaliy G. Goncharov, Xiaofeng Guo, Jian Luo, Yifei Mo*, Feng Jiao*, Liangbing Hu*

*Corresponding author. Email: binghu@umd.edu (L.H.); jiao@udel.edu (F.J.); yfmo@umd.edu (Y.M.)

Published 28 January 2022, *Sci. Adv.* **8**, eabm4322 (2022)
DOI: 10.1126/sciadv.abm4322

The PDF file includes:

Other Supplementary Material for this manuscript includes the following:

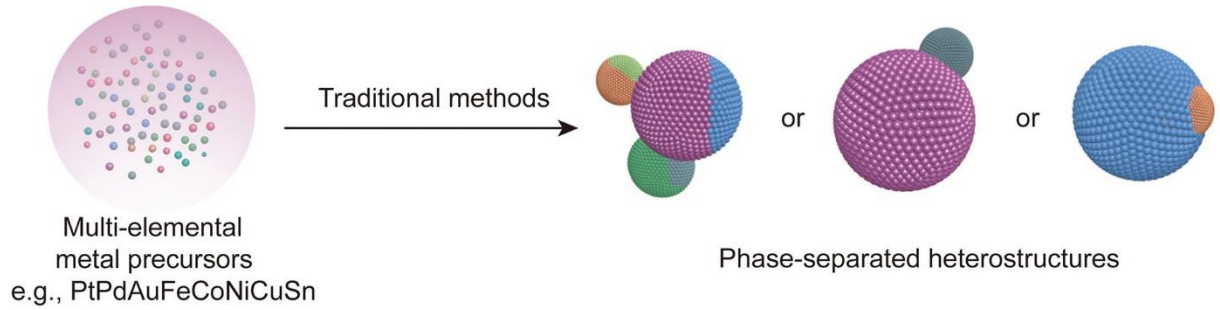

Fig. S1. A schematic diagram of multi-elemental particles with phase-separated heterostructure made by a traditional thermal reduction method. The thermal reduction method involves heating at ~1100 K for 3 h in Ar/H_2 flow (ratio 95:5) within a furnace.

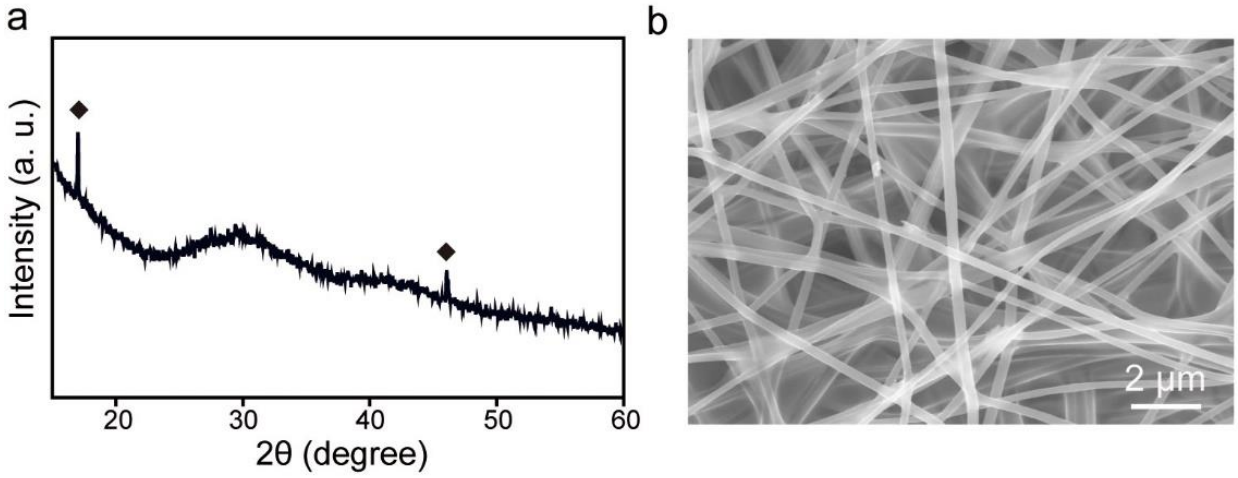

Fig. S2. 8-element salt precursors coated on carbon substrates characterization. a. XRD profile. **b**. The SEM image. XRD pattern and SEM image confirm a uniform precursor loading on the carbon substrates, which is crucial to achieve the desired nanoparticle compositions via the Joule-heating method.

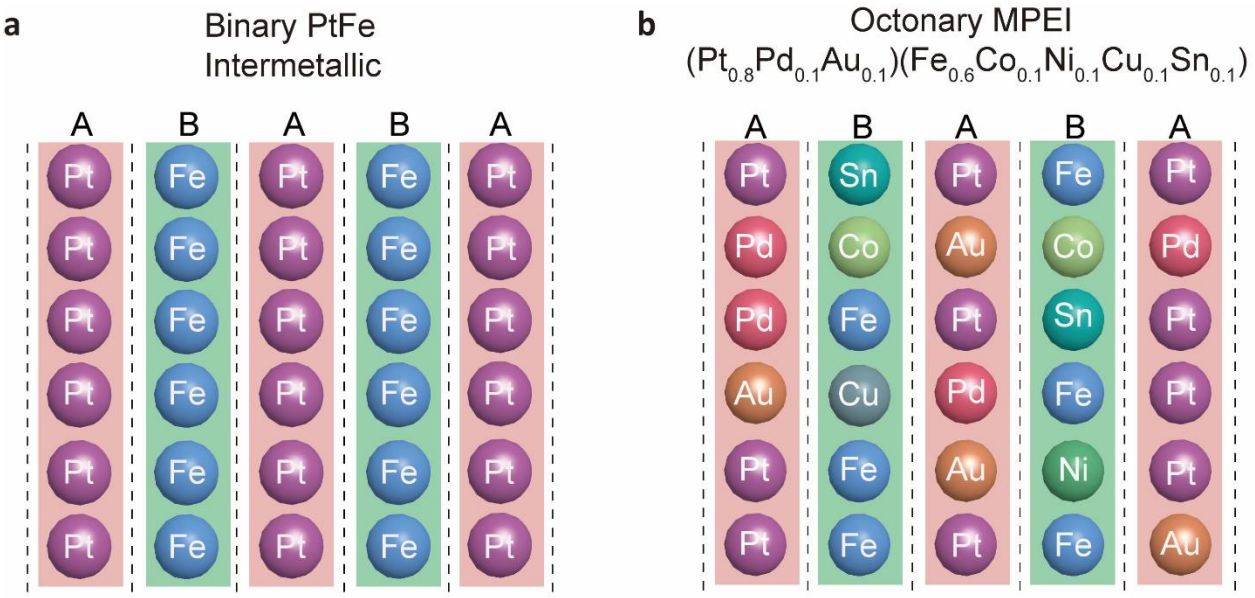

Fig. S3. The binary and octonary ordered $L1_0$ intermetallic structures along the [110] direction. a, For the binary $L1_0$ PtFe intermetallic structure, sub-lattice A and B are each occupied by a single element of Pt or Fe. **b,** For the octonary $(Pt_{0.8}Pd_{0.1}Au_{0.1})(Fe_{0.6}Co_{0.1}Ni_{0.1}Cu_{0.1}Sn_{0.1})$ intermetallic, the noble metal atoms Pt, Pd, and Au randomly distribute in sub-lattice A and the non-noble metal atoms Fe, Co, Ni, Cu, and Sn randomly distribute in sub-lattice B to form the layered $L1_0$ intermetallic structure.

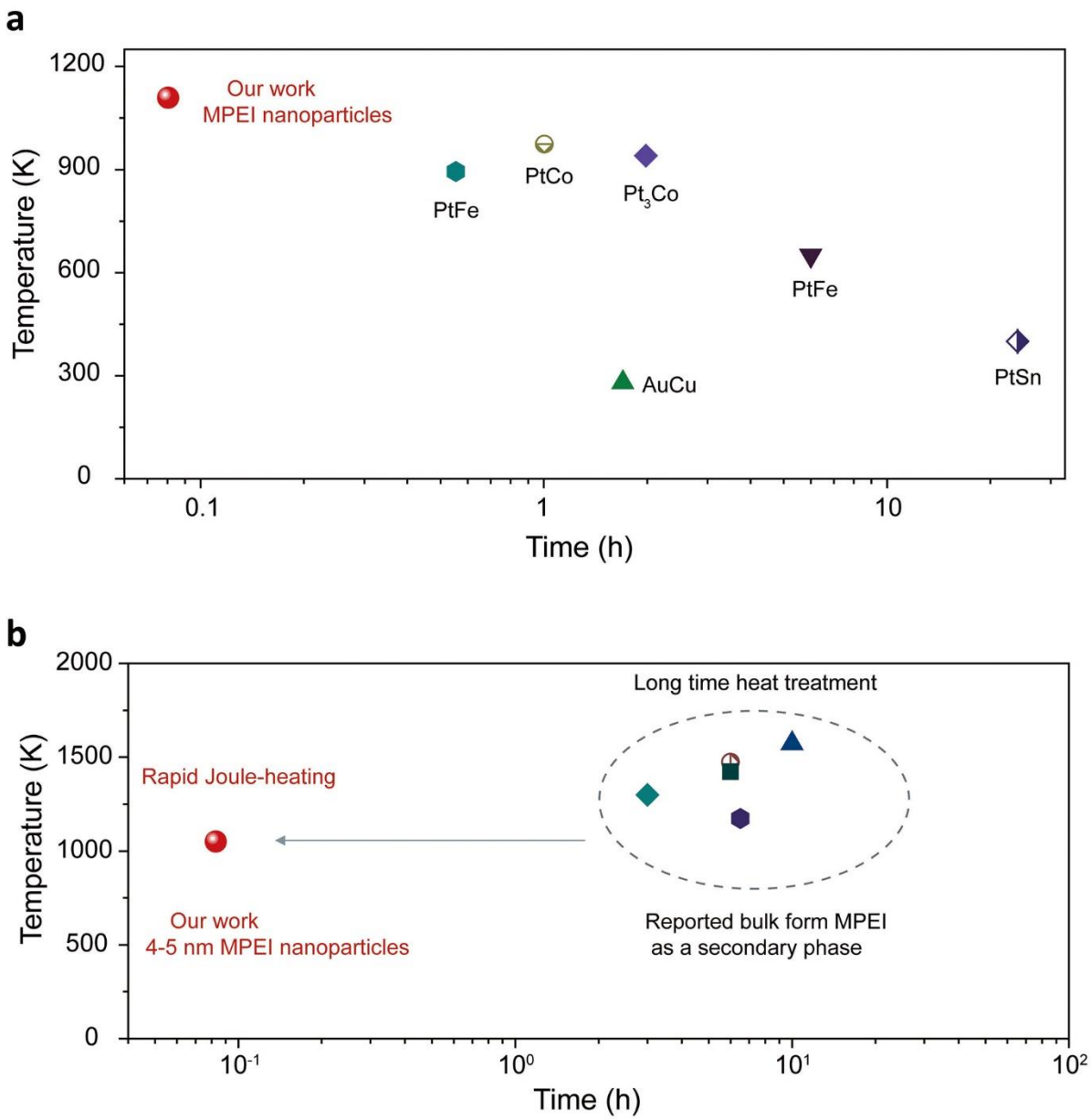

Fig. S4. Comparison of our MPEI nanoparticles with reported MPEIs. a, Comparison of reported binary and ternary intermetallic nanoparticles *(4-6, 12, 42-44)* with our MPEI nanoparticles in terms of their synthesis temperature and time. Conventional intermetallic nanoparticles have been limited to binary or ternary in the literature. Our unique process therefore opens up a new material space for nanoscale MPEIs. **b,** Comparison of reported bulk MPEIs *(45-49)* with our MPEI nanoparticles in terms of their synthesis temperature and time. The bulk intermetallics reported in literature are synthesized via traditional methods, which use long heating durations (e.g., several hours) with slow cooling rates ($< 10^2$ K/s).

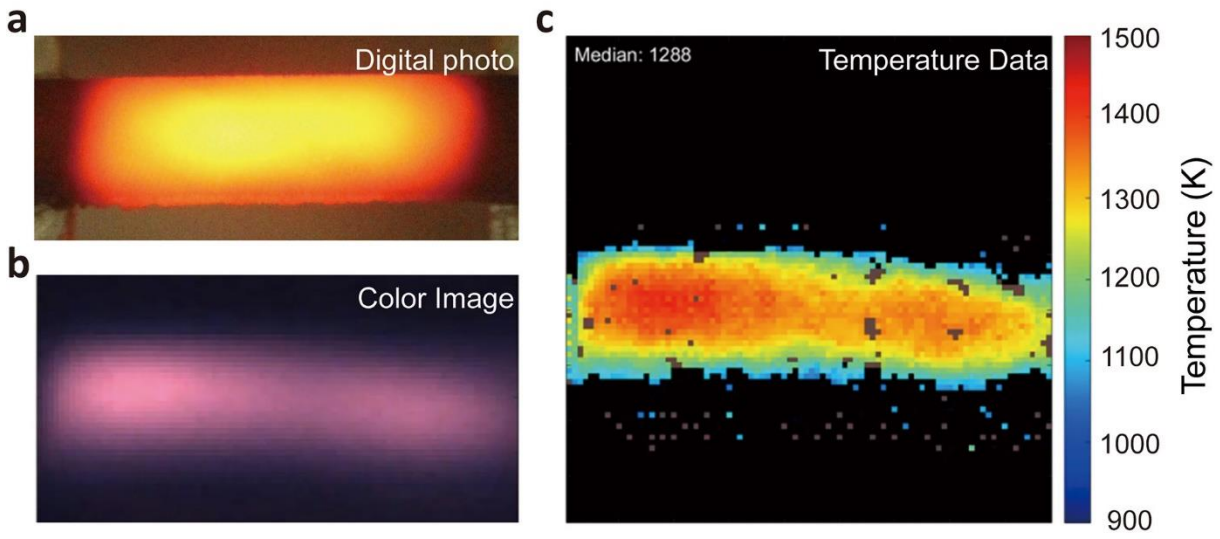

Fig. S5. Digital photo and emitted light spectrum captured by a high-speed camera. a, A digital photo of the carbon substrate during Joule-heating. **b,** The color image of the emitted light spectrum captured by a high-speed camera. **c,** The carbon substrate features a uniform spatial temperature distribution.

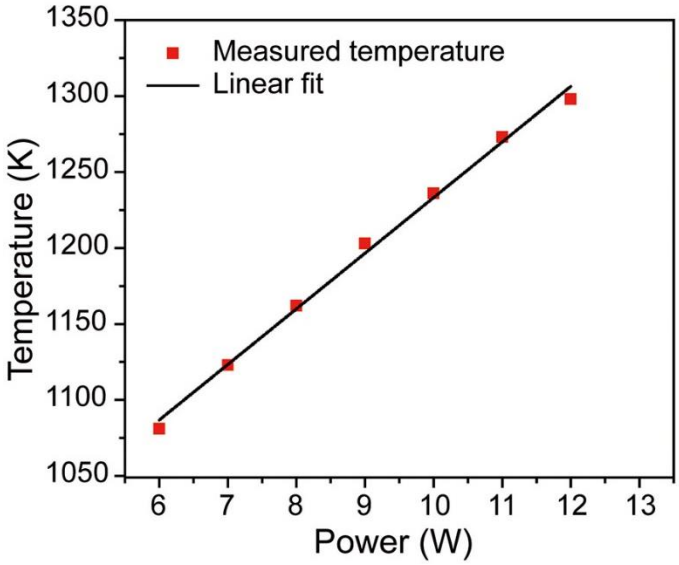

Fig. S6. The measured temperature distribution across the carbon substrate achieved by Joule-heating. We can control the heating temperature by tuning the electrical input signal. When the power is ~6.5 W, the temperature of the carbon substrate can be as high as ~1100 K.

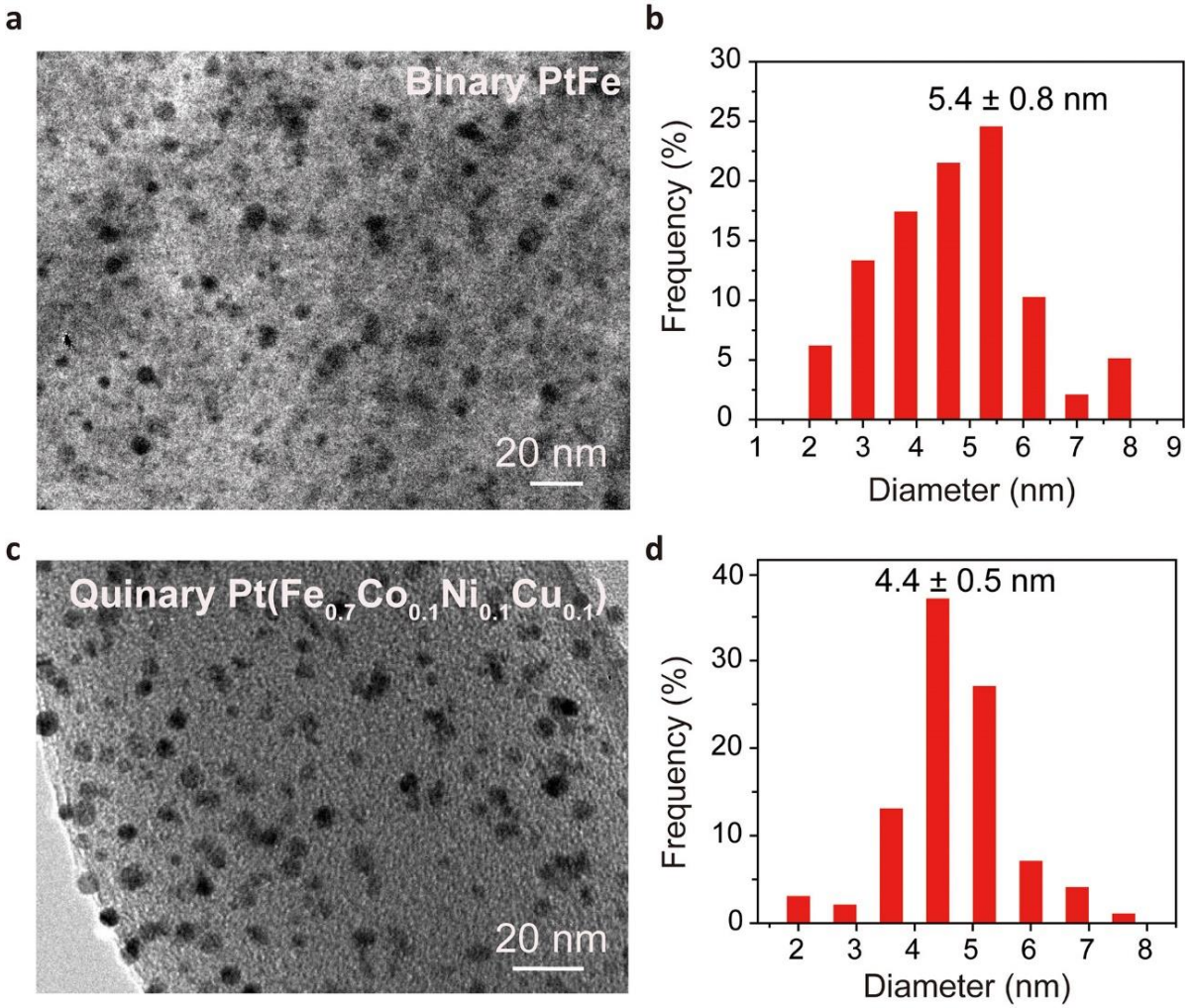

Fig. S7. TEM images and the diameter distributions of the binary and quinary nanoparticles. **a,** TEM image of the binary PtFe nanoparticles on the carbon substrate. **b,** Histogram of the nanoparticle diameter distribution based on the TEM image shown in **a**, revealing a small average diameter (5.4 nm) and narrow size distribution (± 0.8 nm) across the carbon substrate. **c,** TEM image of the quinary $Pt(Fe_{0.7}Co_{0.1}Ni_{0.1}Cu_{0.1})$ nanoparticles on the carbon substrate. **d,** Histogram of the nanoparticle diameter distribution based on the TEM image shown in **c**, revealing the quinary $Pt(Fe_{0.7}Co_{0.1}Ni_{0.1}Cu_{0.1})$ MPEI nanoparticles possess a small average diameter (4.4 nm) and narrow size distribution (± 0.5 nm) across the carbon substrate.

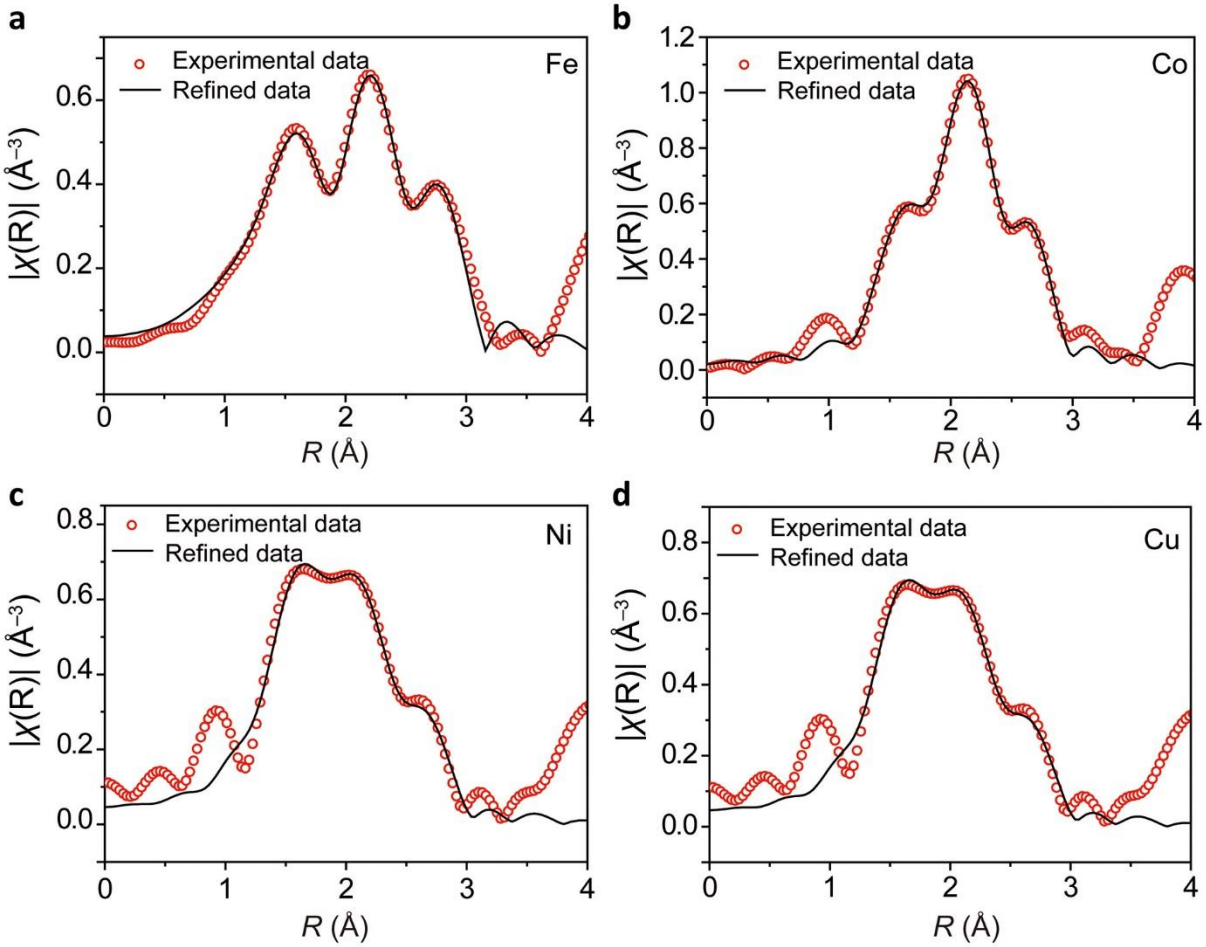

Fig. S8. EXAFS spectra of the quinary Pt($Fe_{0.7}Co_{0.1}Ni_{0.1}Cu_{0.1}$) MPEI nanoparticles. The spectra include the **a,** Fe K-edge, **b,** Co K-edge, **c,** Ni K-edge, and **d,** Cu K-edge.

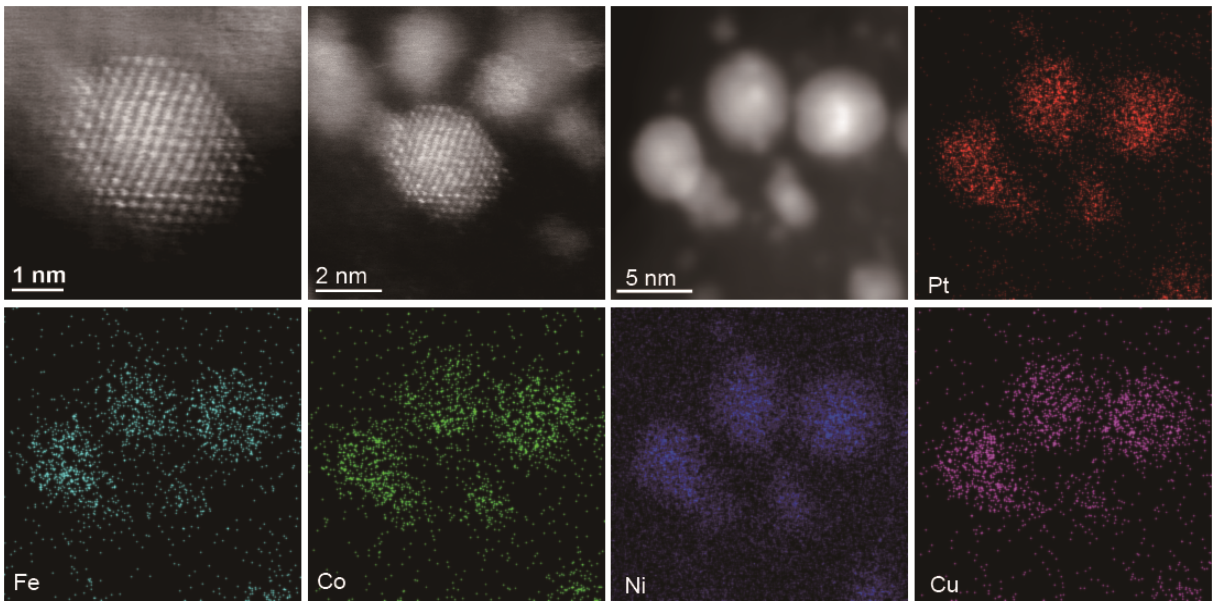

Fig. S9. STEM images and EDX mapping of Pt($Fe_{0.25}Co_{0.25}Ni_{0.25}Cu_{0.25}$) nanoparticles. The different contrast of the alternating layers in the STEM images and homogeneous elemental distribution confirm that atomically ordered quinary Pt(FeCoNiCu) MPEIs can be achieved at different composition ratios (vs. 1:0.7:0.1:0.1:0.1, as shown in Fig. 2C).

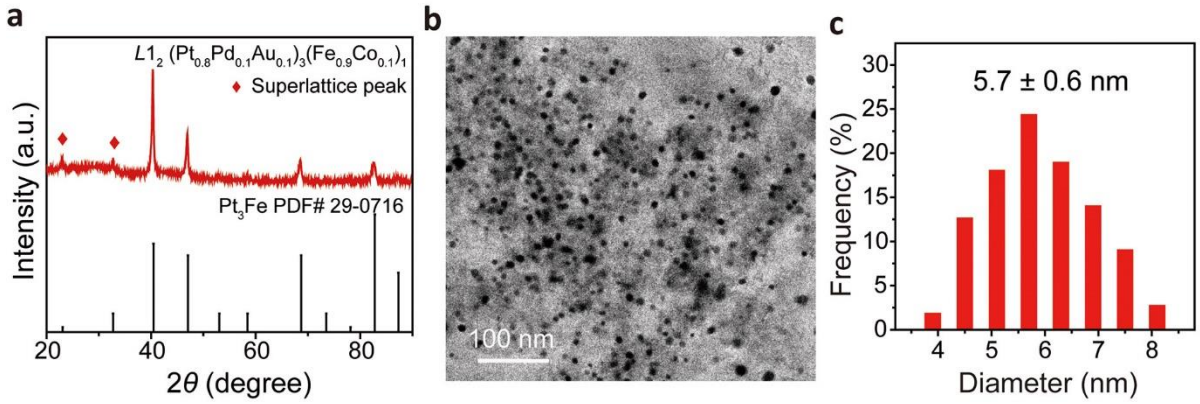

Fig. S10. XRD and TEM characterization of quinary $(Pt_{0.8}Pd_{0.1}Au_{0.1})_3(Fe_{0.9}Co_{0.1})$ nanoparticles. a, XRD patterns of the quinary MPEI $(Pt_{0.8}Pd_{0.1}Au_{0.1})_3(Fe_{0.9}Co_{0.1})$ nanoparticles with an $L1_2$ ordered structure synthesized using the Joule-heating method. **b,** TEM of the quinary $L1_2$ $(Pt_{0.8}Pd_{0.1}Au_{0.1})(Fe_{0.9}Co_{0.1})$ nanoparticles on the carbon substrate. **c,** Histogram of the nanoparticle diameter distribution based on the TEM image shown in **b**, revealing the quinary $L1_2$ $(Pt_{0.8}Pd_{0.1}Au_{0.1})(Fe_{0.9}Co_{0.1})$ nanoparticles possess a small average diameter (5.7 nm) and narrow size distribution (± 0.6 nm) across the carbon substrate.

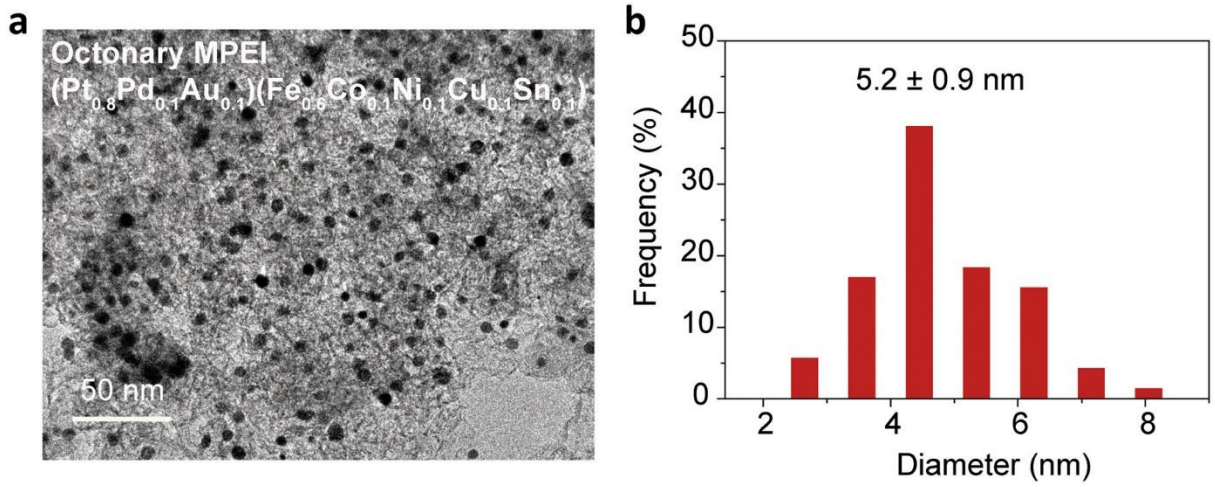

Fig. S11. Characterization of octonary MPEI nanoparticles on the carbon substrate. a, TEM image of octonary $(Pt_{0.8}Pd_{0.1}Au_{0.1})(Fe_{0.6}Co_{0.1}Ni_{0.1}Cu_{0.1}Sn_{0.1})$. **b,** Histogram of the nanoparticle diameter distribution based on the TEM image shown in **a**, revealing a small average diameter (5.2 nm) and narrow size distribution (± 0.9 nm) across the carbon substrate.

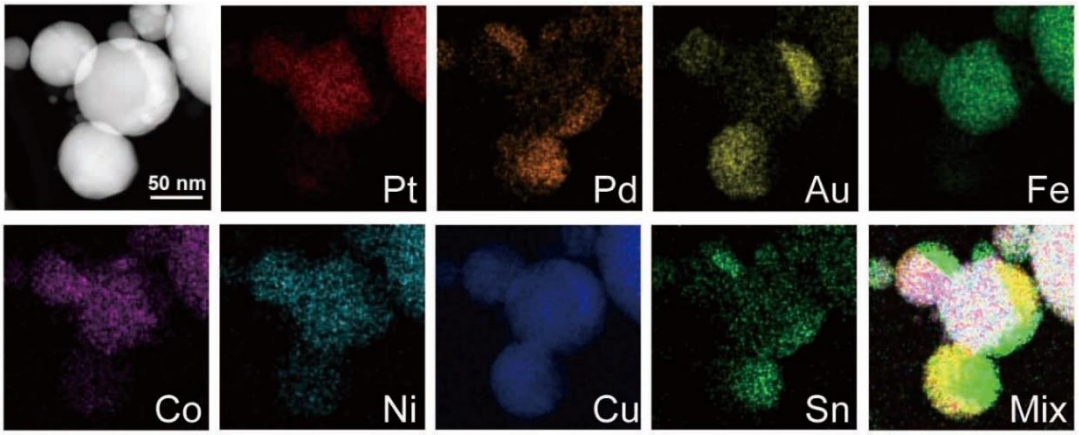

Fig. S12. A HAADF-STEM image and EDX mapping of octonary particle made by a traditional thermal annealing method. The octonary $Pt_{0.8}Pd_{0.1}Au_{0.1}Fe_{0.6}Co_{0.1}Ni_{0.1}Cu_{0.1}Sn_{0.1}$ particles show the phase separation structure.

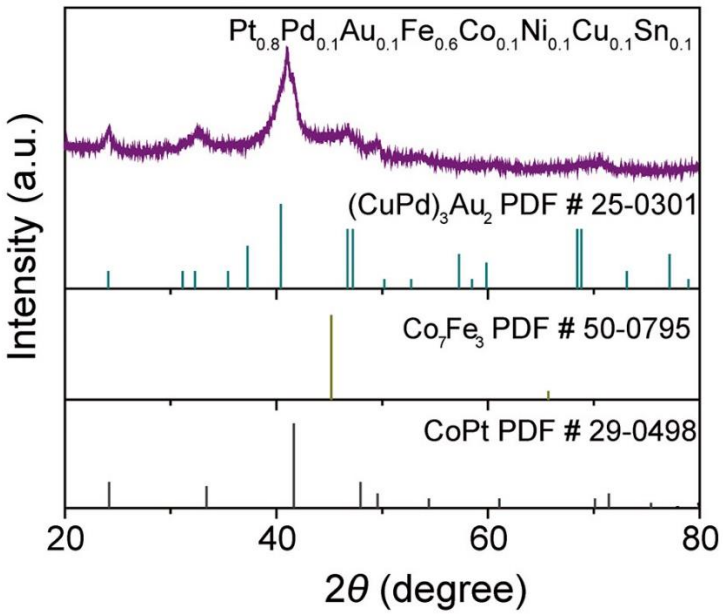

Fig. S13. XRD patterns of an octonary sample synthesized by the traditional annealing method. The octonary $(Pt_{0.8}Pd_{0.1}Au_{0.1})(Fe_{0.6}Co_{0.1}Ni_{0.1}Cu_{0.1}Sn_{0.1})$ composition showed heterostructures with multiple phases, including $(CuPd)_3Au_2$, Co_7Fe_3, and CoPt. Thus, the traditional thermal annealing method cannot be used for synthesizing octonary MPEIs.

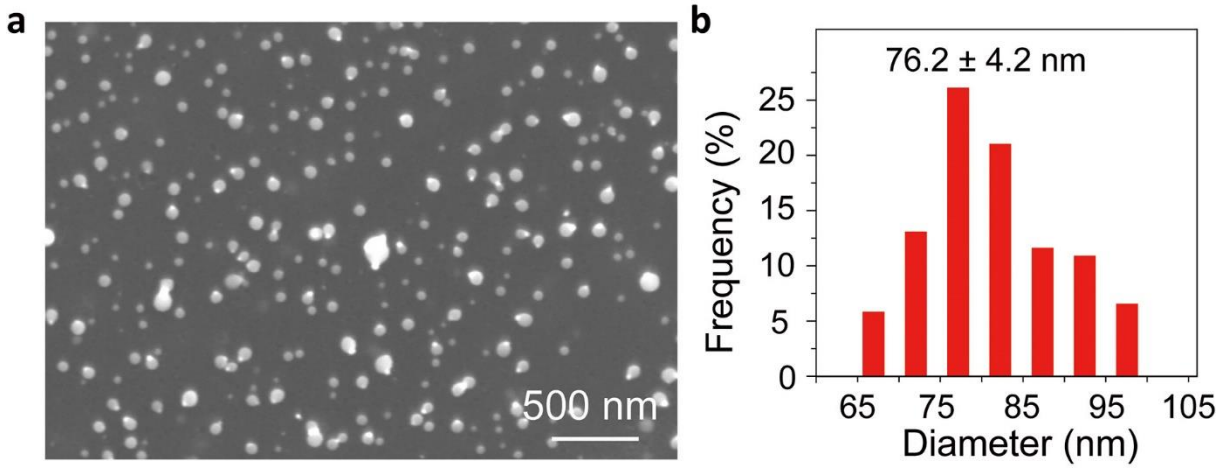

Fig. S14. SEM characterization of the octonary sample synthesized by traditional annealing. **a,** SEM image of $Pt_{0.8}Pd_{0.1}Au_{0.1}Fe_{0.6}Co_{0.1}Ni_{0.1}Cu_{0.1}Sn_{0.1}$ and **b,** the corresponding histogram of the particle diameter distribution, which featured an average particle size of 76.2 ± 4.2 nm.

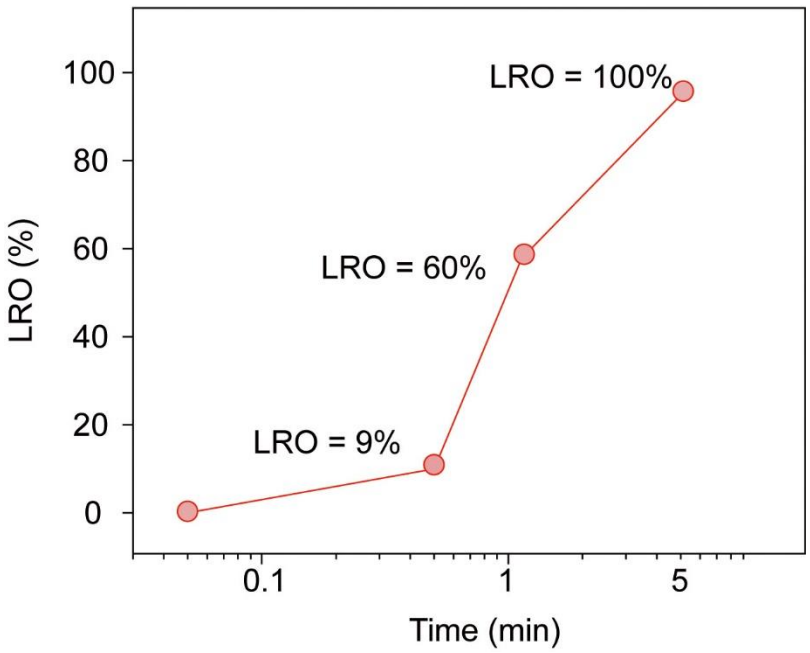

Fig. S15. The LRO of the quinary Pt($Fe_{0.7}Co_{0.1}Ni_{0.1}Cu_{0.1}$) as a function of the heating time. The LRO increases with the heating time. For the quinary Pt($Fe_{0.7}Co_{0.1}Ni_{0.1}Cu_{0.1}$) composition, 5 min heating is sufficient to achieve the fully ordered intermetallic structure (LRO = 100%).

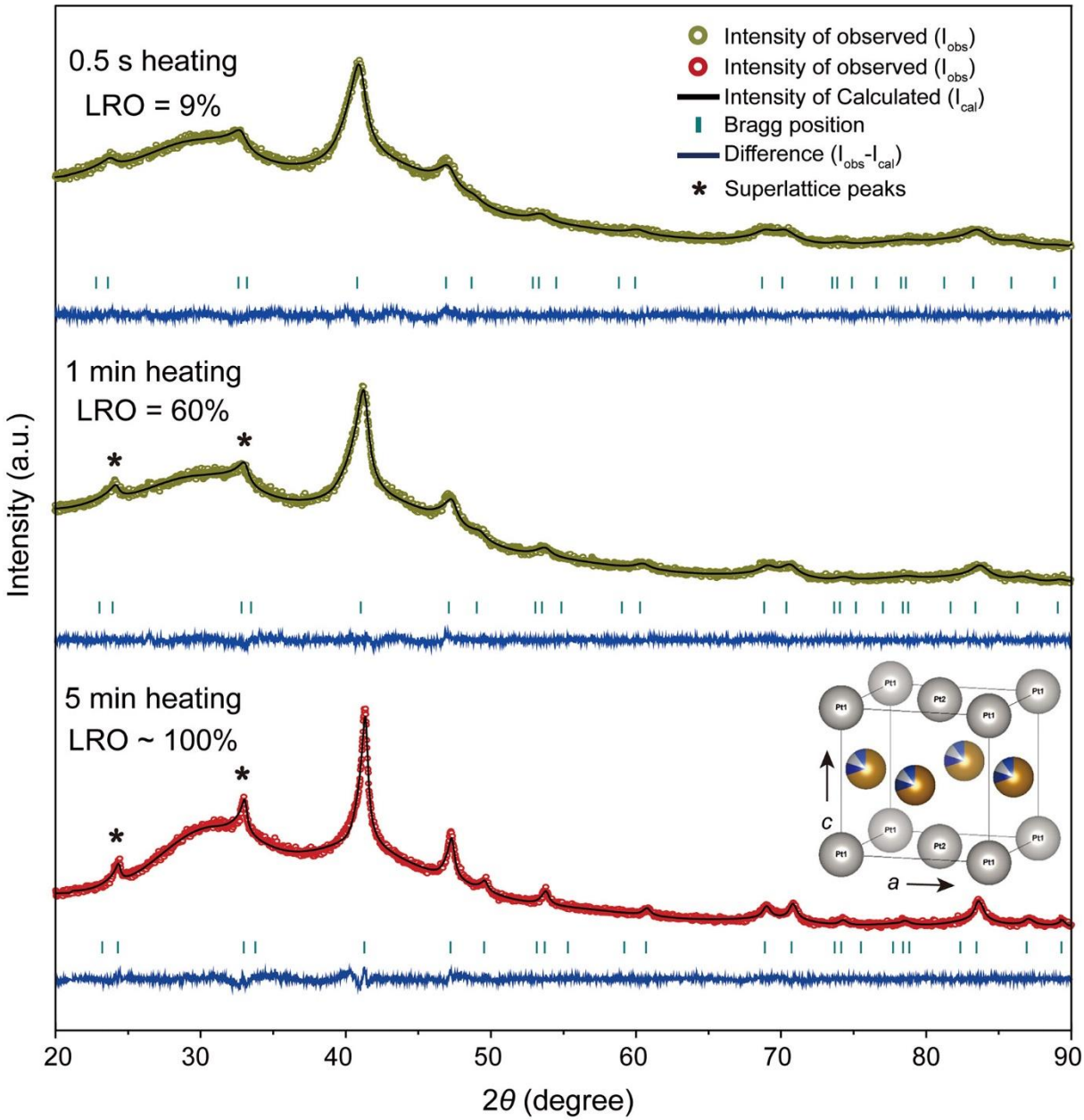

Fig. S16. The Rietveld refinement of the XRD patterns for the quinary MPEI nanoparticles. The nanoparticles synthesized by heating at ~1100 K for 0.5 s, 1 min, and 5 min (from top to bottom, respectively). ∗ denotes the $L1_0$ superlattice peaks. The idealized XRD pattern has 100% $L1_0$-ordering. The structural pattern shown in the inset is the exported structure of the $Pt(Fe_{0.7}Co_{0.1}Ni_{0.1}Cu_{0.1})$ MPEI, showing that Pt occupies one sub-lattice and Fe, Co, Ni, and Cu occupy another sub-lattice.

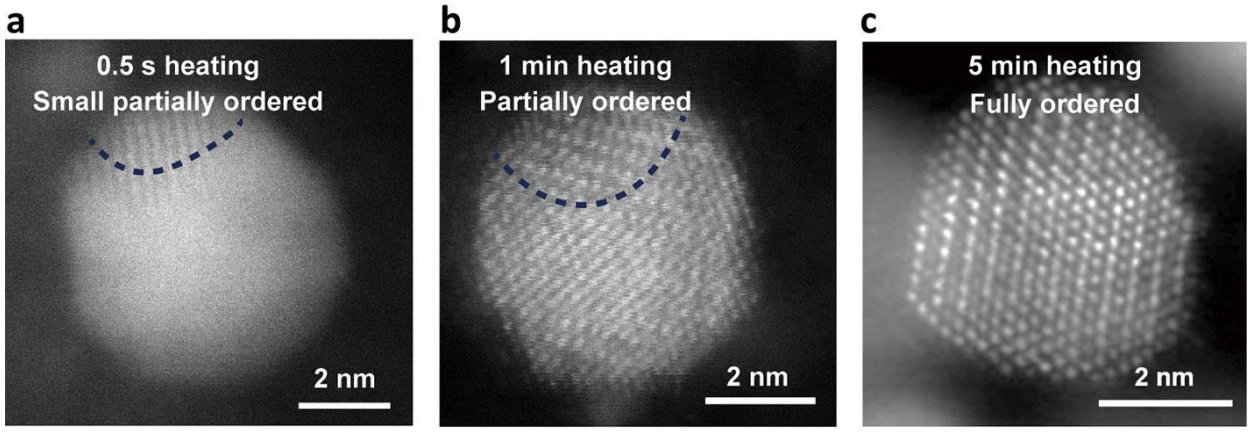

Fig. S17. STEM images showing the evolution of quinary nanoparticles held at a temperature of ~1100 K via Joule-heating for different amounts of time. a, 0.5 s, **b,** 1 min, and **c,** 5 min. **a,** The quinary Pt($Fe_{0.7}Co_{0.1}Ni_{0.1}Cu_{0.1}$) sample made by 0.5 s heating duration shows a small partially ordered structure. **b,** The sample made by 1 min heating shows slightly more but still partial ordering. **c,** The sample made by 5 min heating features a fully ordered structure with alternating layers of FeCoNiCu and Pt columns along the [001] axis.

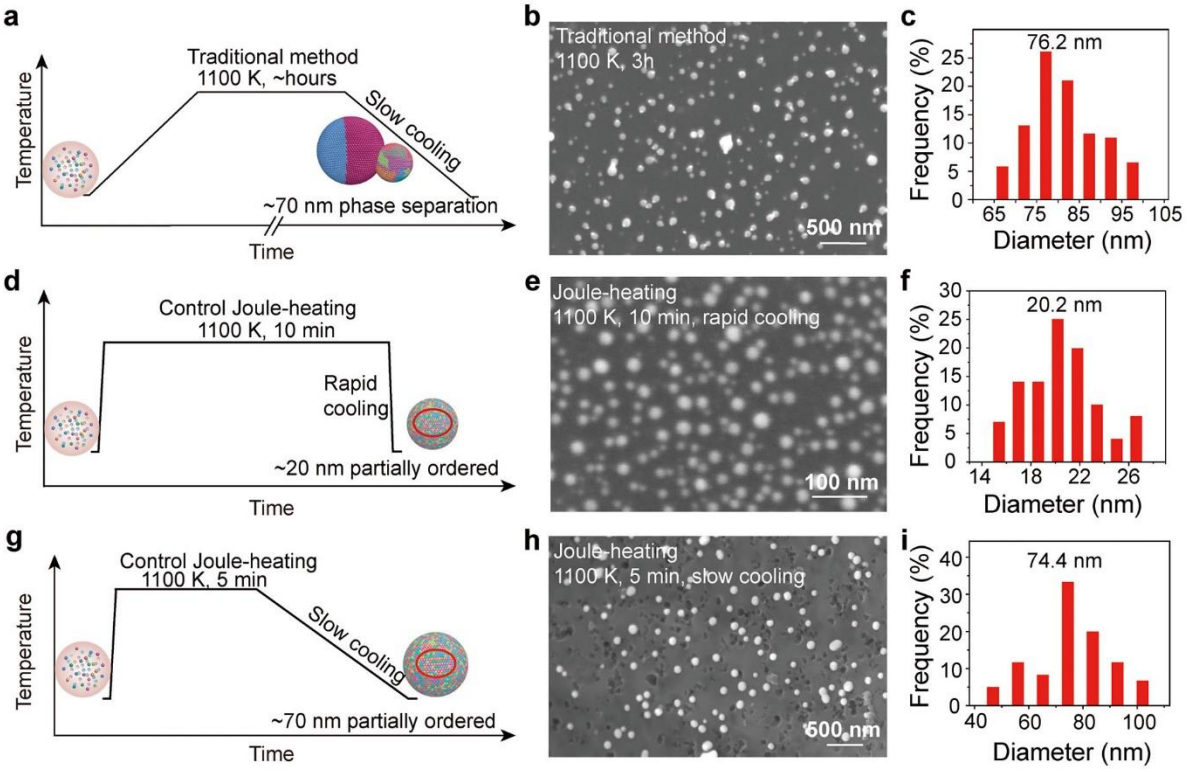

Fig. S18. The morphology, particle size, and XRD of the control samples. a, Schematic illustration of the traditional synthesis process (~1100 K, 3 h), and **b, c** the corresponding SEM image and histogram of the particle size distribution of octonary $Pt_{0.8}Pd_{0.1}Au_{0.1}Fe_{0.6}Co_{0.1}Ni_{0.1}Cu_{0.1}Sn_{0.1}$ particles synthesized by the method shown in **a**. **d,** Schematic illustration of the synthesis process of Joule-heating at ~1100 K for 10 min, with rapid heating/cooling, and **e, f** the corresponding SEM image and histogram of the particle size distribution of the resulting octonary particles. **g,** Schematic illustration of the synthesis process of Joule-heating at ~1100 K for 5 min, with fast heating but slow cooling rates, and **h, i** the corresponding SEM image and histogram of the particle size distribution of the resulting octonary particles. The morphology, particle size, and XRD of the above control samples demonstrate that the traditional annealing results in a particle size of ~60 nm. HAADF imaging and STEM EDX mapping of the particles further show a phase-separated structure. In comparison, the Joule-heating control samples result in a particle size of 20 nm or 70 nm with a partially ordered structure. The Joule-heating method allows for the critical two-step transitions necessary to produce MPEI nanoparticles, which unattainable by other heating processes.

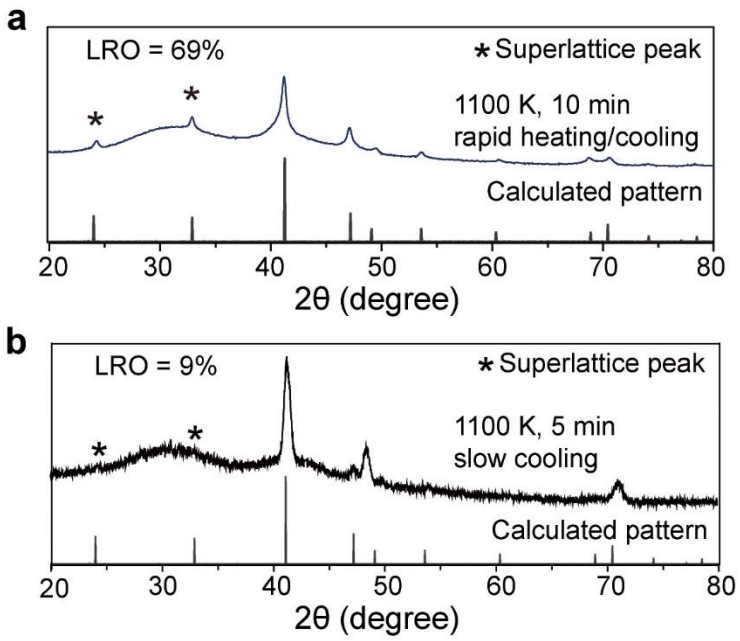

Fig. S19. The XRD patterns of the particles synthesized at ~1100 K. **a,** 10 min heating duration with rapid Joule-heating/cooling rates and **b,** 5 min heating duration with a slowing cooling rate. The large particles size of sample **a** (20.2 nm, Fig. S18e, f) and sample **b** (74.4 nm, Fig. S18h, i) feature the LRO value of 69% and 9%, respectively. Thus, the LRO decreases with the particle size, irrespective of the particle synthesis method (slow cooling or longer heating time).

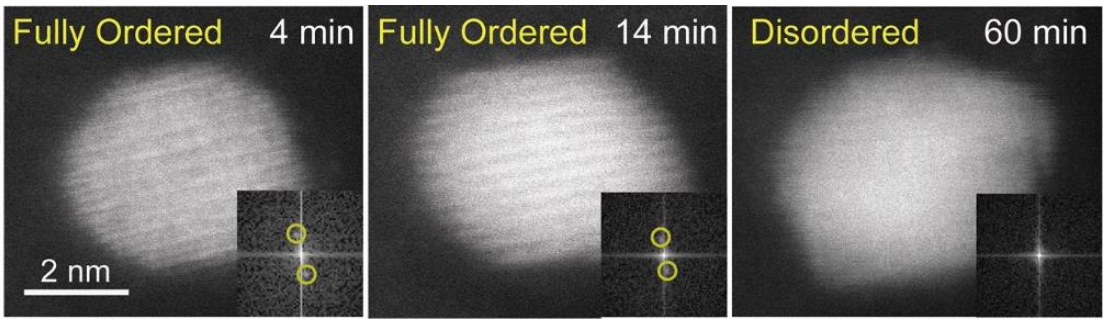

Fig. S20. Time-resolved HAADF-STEM images of a binary PtFe. The images show the phase evolution (from fully ordered transition to disordered structure) of a binary PtFe nanoparticle being heated at ~1100 K over a period of 60 min (the insets are the corresponding Fast Fourier Transform results).

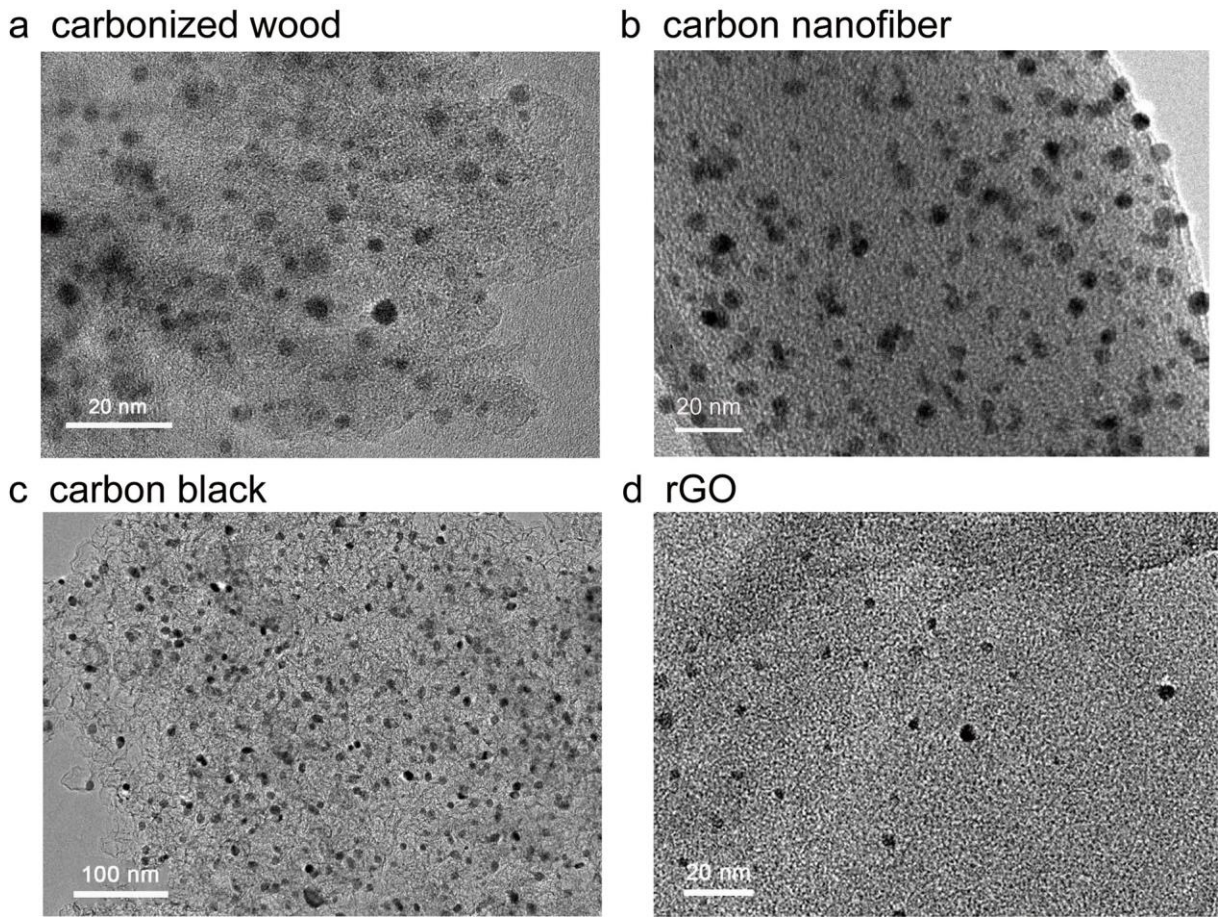

Fig. S21. TEM images of octonary MPEI nanoparticles supported on different carbon substrates. a, carbonized wood; **b**, carbon nanofiber; **c**, carbon black; **d**, rGO. Uniform distribution of the nanoparticles through the carbon substrates indicates the Joule-heating method is a general method for multiple carbon substrates.

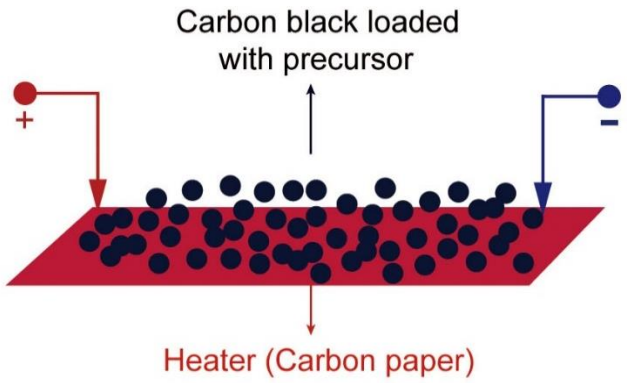

Fig. S22. MPEI nanoparticles synthesis on Ketjen black carbon support through radiation heating. We fabricated octonary MPEI nanoparticles on Ketjen black carbon through radiation-based heating to demonstrate the scalable synthesis. Good scalability can be achieved via the following: 1) The precursor loading can be easily achieved through a “coating-drying” method; 2) Extension of the heating mode from in-contact Joule-heating to radiation heating.

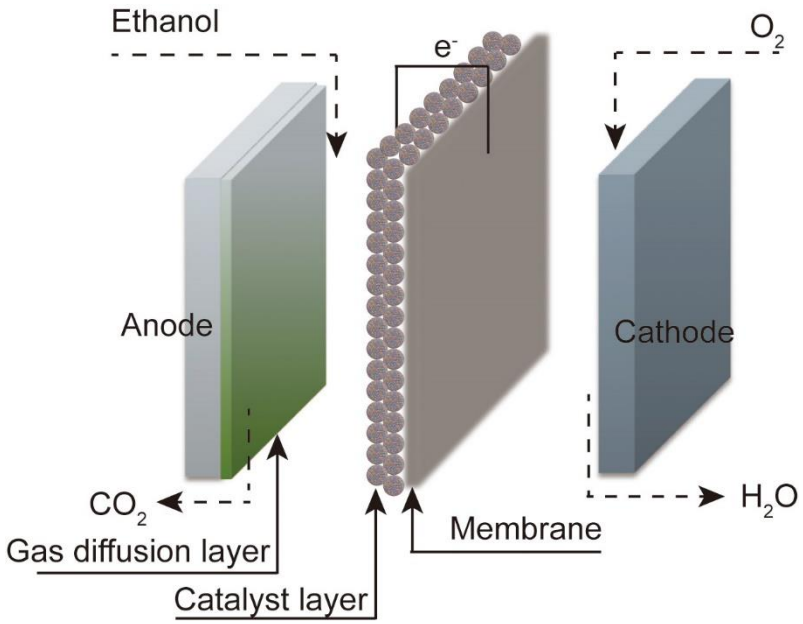

Fig. S23. Schematic illustration of the MPEI nanoparticles as a catalyst for direct ethanol fuel cells, which employ EOR. Ethanol is oxidized at the anode, while oxygen is reduced at the cathode. Protons are transported across the proton exchange membrane. Electrons are transported through the external circuit from the anode to the cathode, providing power to the load. In this configuration, we used our octonary $(Pt_{0.8}Pd_{0.1}Au_{0.1})(Fe_{0.6}Co_{0.1}Ni_{0.1}Cu_{0.1}Sn_{0.1})$ MPEI nanoparticles as the anode catalyst.

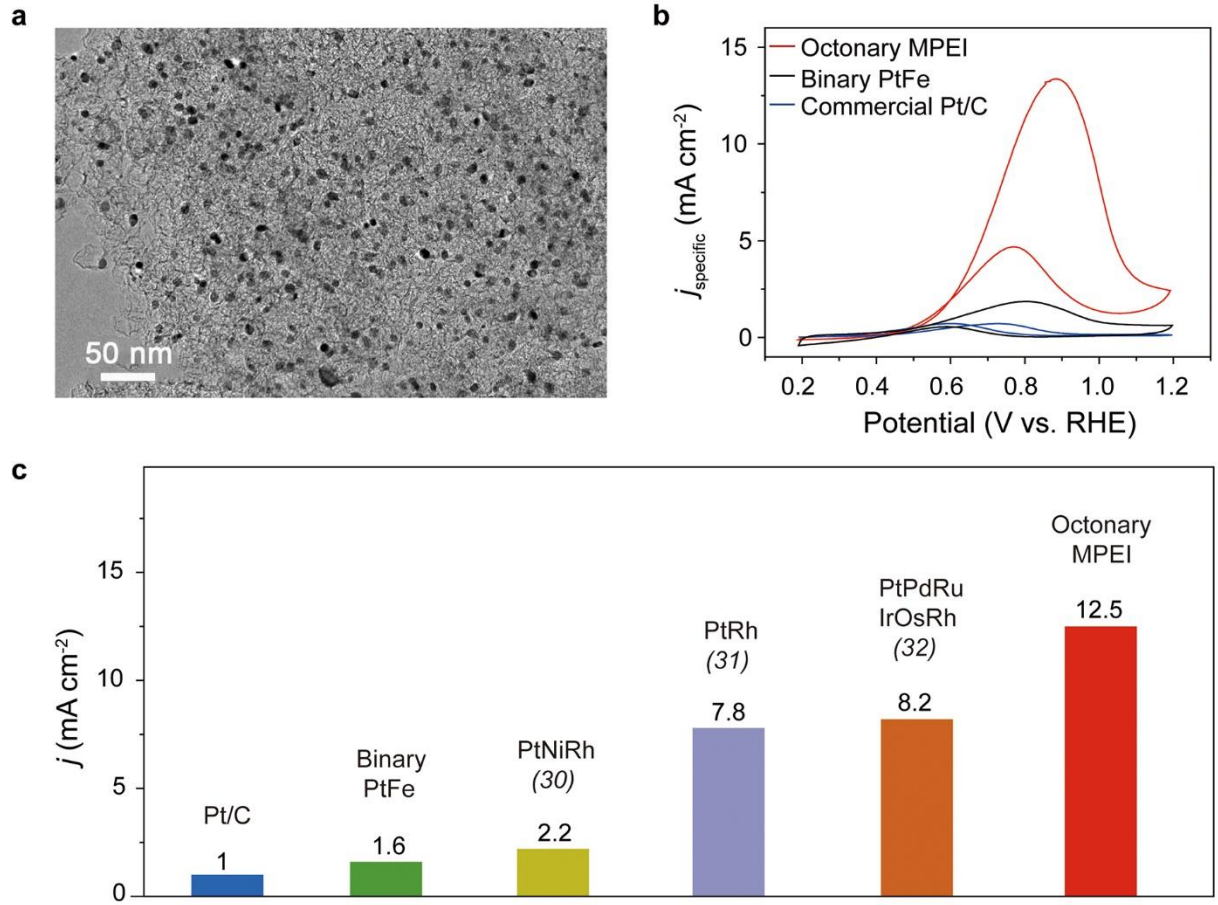

Fig. S24. EOR performance of the octonary MPEI nanoparticles. a, TEM image of the supported octonary $(Pt_{0.8}Pd_{0.1}Au_{0.1})(Fe_{0.6}Co_{0.1}Ni_{0.1}Cu_{0.1}Sn_{0.1})$ MPEI nanoparticles on carbon black. **b,** EOR CV curves of the octonary $(Pt_{0.8}Pd_{0.1}Au_{0.1})(Fe_{0.6}Co_{0.1}Ni_{0.1}Cu_{0.1}Sn_{0.1})$ MPEI nanoparticles, binary PtFe intermetallic nanoparticles, and commercial Pt/C catalyst tested in 1 M KOH and 1 M EtOH. **c,** Comparison of the catalytic activity (current density of EOR) between the MPEI nanoparticle materials and previously reported Pt-based catalyst materials *(30-32)*. To investigate their catalytic ability, we prepared the octonary MPEI nanoparticles on a carbon black substrate, which enable high-rate and high-volume production of quality nanoparticles and easy to cast on carbon paper as a catalytic electrode. TEM imaging confirms the uniform size distribution (~5 nm) of the resulting MPEI nanoparticles (Fig. S24a). The octonary MPEI nanoparticles demonstrate improved EOR activity that is 8- and 12-times higher than the binary PtFe intermetallic and commercial Pt/C catalyst, respectively, as evidenced by cyclic voltammetry (CV; Fig. S24b). This EOR activity is also among the best reported in the literature *(30-32)* (Fig. S24c).

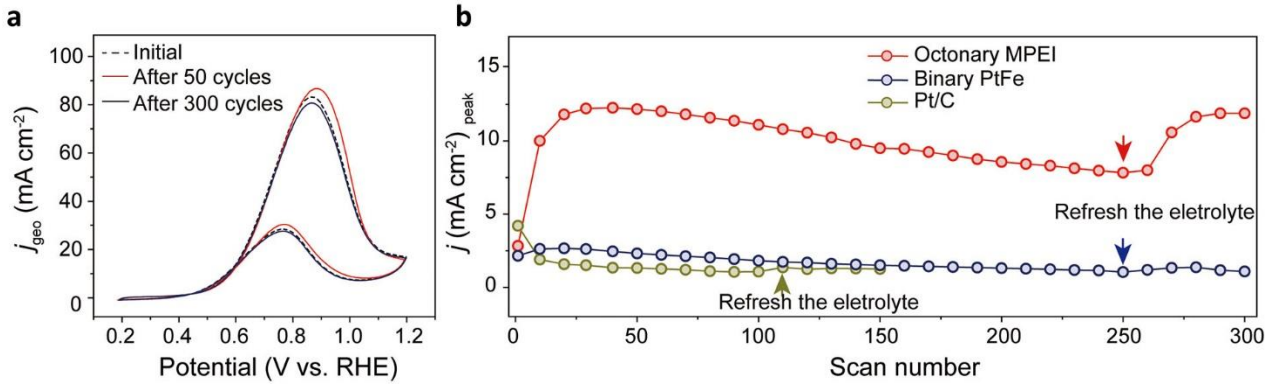

Fig. S25. EOR stability performance of the octonary MPEI nanoparticles. a, Comparison of the CV curves before and after 300 cycles of EOR catalysis using the octonary $(Pt_{0.8}Pd_{0.1}Au_{0.1})(Fe_{0.6}Co_{0.1}Ni_{0.1}Cu_{0.1}Sn_{0.1})$ MPEI nanoparticles. **b,** Comparison of the cycling stability (peak current density at different CV cycles) between the octonary $(Pt_{0.8}Pd_{0.1}Au_{0.1})(Fe_{0.6}Co_{0.1}Ni_{0.1}Cu_{0.1}Sn_{0.1})$ MPEI nanoparticles, binary PtFe intermetallic, and commercial Pt/C catalyst. For the octonary MPEI and binary PtFe intermetallic, the electrolyte was refreshed at the 250th cycle. For the commercial Pt/C catalyst, the electrolyte was refreshed at the 110th cycle. The current is normalized to the electrochemically active surface area (ECSA) of the electrode. The ECSA of the octonary MPEI, binary PtFe, and Pt/C is 40.4 m^2 g^{-1}, 20.3 m^2 g^{-1}, and 12.8 m^2 g^{-1}, respectively. The structural and chemical stability of the octonary MPEI nanoparticles also contributes to their excellent durability during long-term catalytic operation (300 CV cycles; Fig. S25a), comparable to previous literature reports *(30-32)*. Despite having a slight decay after 250 CV cycles, the activity of the octonary MPEI nanoparticle catalyst can be almost fully recovered after refreshing the electrolyte (Fig. S25b), indicating the activity decay was likely due to mass transport limitations as a result of ethanol consumption rather than degradation of the catalyst. For comparison, the binary PtFe intermetallic demonstrates only partial recovery (~47%) of the catalytic activity after refreshing the electrolyte at the 250th cycle, compared with the original activity. Meanwhile, the commercial Pt/C catalyst displays even lower recovery (~31%) of the catalytic activity after refreshing the electrolyte at the 110th cycle. Thus, the octonary MPEI nanoparticles function as an exceptional EOR catalyst with high activity and stability, which could be attributed to the material's multi-elemental composition, ordered intermetallic structure, and nanosize.

Table S1. Binary and ternary ordered intermetallic nanoparticles reported in the literature.

Year		Composition	Ref.
1989	Binary	PtFe	*(6)*
2009		PtCo	*(42)*
2013		Pt_3Co	*(4)*
2014		PtSn	*(43)*
2014		AuCu	*(5)*
2018		PtFe	*(44)*
2019	Ternary	PtSnBi	*(12)*

Table S2. Comparison of reported MPEIs as a secondary phase in high-entropy matrices with our MPEI nanoparticles.

Composition	Phase	Size			Ref.
		Grain	precipitation	Model	
Fe-21Mn-10Al-1C-5Ni (wt.%)	*Austenite (86%)*	1.5 μm	-	30 kg ingot	*(45)*
	B2	500 nm	0.14 μm		
	$D0_3$ (in B2)	4 nm	-		
Fe-13.5Cr-4.7Al-2.1Mo-0.5Nb-0.8Ta-0.2Zr (wt. %)	*BCC*	1.2 μm	-	26.0×5.0 × 1.5	*(46)*
	Laves	150-200 nm	500 nm		
Fe-15Mn-10Al-0.8C-5Ni	*Austenite*	3.5 –4.5 μm	-	25 ×6.25 × 1	*(47)*
	B2	350 nm	60 nm		
(FeCoNi)86-Al7Ti7	*FCC*	40~50 μm	-	5 × 10 × 50	*(48)*
	$L1_2$	30~50 nm	-		
Co-Cr-Fe-Ni-Nb	*FCC*	0.5 μm	-	Diameter 3	*(49)*
	Laves	200 nm	-		
$(Pt_{0.8}Pd_{0.1}Au_{0.1})(Fe_{0.6}Co_{0.1}Ni_{0.1}Cu_{0.1}Sn_{0.1})$	*Single $L1_0$ phase*	Nanoparticle 4~5 nm			This work

Table S3. Fitting parameters of the Fourier transition of the first shell of the EXAFS spectra.

Sample	Edge	Scatter	Coordination number	R_0 (Å)	$\sigma^2/10^{-3}$ Å^2	E_0/eV
Quinary ordered $Pt(Fe_{0.7}Co_{0.1}Ni_{0.1}Cu_{0.1})$	Pt L_3	Pt-Pt	6(1)	2.713(8)	7(1)	4.5(9)
		Pt-M	3.0(8)	2.65(1)	8(2)	4.5(9)
	Fe K	Fe-Pt	6(1)	2.67(1)	7(1)	-4(1)
		Fe-Cu	1.2(4)	2.69(3)	7(1)	-4(1)
	Cu K	Cu-Pt	3(1)	2.63(2)	10(2)	-5(2)
		Cu-Fe	1.0(4)	2.67(3)	10(2)	-5(2)
	Co K	Co-Pt	6(1)	2.65(1)	7(1)	-9.8(9)
		Co-Ni	2.6(5)	2.61(1)	7(1)	-9.8(9)
	Ni K	Ni-Pt	4(2)	2.66(4)	10(4)	-9(4)
		Ni-Co	2(1)	2.60(4)	10(4)	-9(4)
Binary ordered PtFe	Pt	Pt-Pt	4.26(5)	2.7214(4)	-	-
		Pt-Fe	3.86(6)	2.6730(2)	-	-

where R_0 is the bond length, and σ^2 is the Debye-Waller factor and reflects the structural disorder in the sample. The ΔE_0 parameter is the absorption edge energy shift, which represents the difference between the experimental E_0 energy and that calculated for the structural model used to fit the spectra.

Table S4 ICP-MS composition of precursors molar ratio and MPEI nanoparticles.

Elements	Pt	Pd	Au	Fe	Co	Ni	Cu	Sn
Precursors		50				50		
molar ratio	40	5	5	30	5	5	5	5
Nanoparticles		53.23				46.77		
ICP-MS	44.53	4.47	4.23	26.61	5.39	5.86	4.64	4.27
Precursors		50				50		
molar ratio	37	6	7	32	4	4	4	6
Nanoparticles		50.71				49.29		
ICP-MS	40.34	5.17	5.19	28.16	5.39	4.88	5.59	5.27

Based on ICP-MS compositional analysis, the elemental compositions of octonary MPEI nanoparticles are slightly different from the molar ratio of the precursors $(Pt_{44.53}Pd_{4.47}Au_{4.23})(Fe_{26.61}Co_{5.39}Ni_{4.88}Cu_{5.59}Sn_{5.27})$=53.23:46.77. We adjust the precursor ratio to compensate for metal slightly loss in the Joule heating synthesis method. The target composition for PtPdAuFeCoNiCuSn is 40:5:5:30:5:5:5:5. When we adjusted the precursor ratio (PtPdAuFeCoNiCuSn salt) to the ratios 37:6:7:32:4:4:4:6 (adding more Pd, Au, Fe, Cu, and Sn to the initial precursor solution to compensate for Pd, Au, Fe, and Sn). After adding more vapor metal precursor to solution, we achieved a final ratio $(Pt_{40.34}Pd_{5.17}Au_{5.19})(Fe_{28.16}Co_{5.39}Ni_{4.88}Cu_{5.59}Sn_{5.27})$=50.71:49.29 that is very close to 1: 1 target.

Table S5. The cell parameters of the quinary Pt(FeCoNiCu) samples synthesized at different heating times after Rietveld refinement.

Sample	Crystallographic parameter (Å)	Atom site (x, y, z)	Occupancy	R_p (%)
0.5 s heating	a 3.848 b 3.848 c 3.718	Fe (0, 0.5, 0.5)	0.7	1.378
		$Pt^{(3)}$ (0, 0.5, 0.5)	0.3	
		$Pt^{(1)}$ (0, 0, 0)	0.7	
		Co (0, 0, 0)	0.1	
		Ni (0, 0, 0)	0.1	
		Cu (0, 0, 0)	0.1	
		$Pt^{(2)}$ (0.5, 0.5, 0)	1	
1 min heating	a 3.853 b 3.853 c 3.710	$Pt^{(1)}$ (0, 0, 0)	1	1.473
		$Pt^{(2)}$ (0.5, 0.5, 0)	0	
		Fe (0, 0.5, 0.5)	0.7	
		Co (0, 0.5, 0.5)	0.1	
		Ni (0, 0.5, 0.5)	0.1	
		Cu (0, 0.5, 0.5)	0.1	
5 min heating	a 3.862 b 3.862 c 3.691	$Pt^{(1)}$ (0, 0, 0)	1	1.529
		$Pt^{(2)}$ (0.5, 0.5, 0)	0	
		Fe (0, 0.5, 0.5)	0.7	
		Co (0, 0.5, 0.5)	0.1	
		Ni (0, 0.5, 0.5)	0.1	
		Cu (0, 0.5, 0.5)	0.1	

Table S6. The thermochemical reactions used for the calculation of the corrected enthalpies (deducting the contribution of the carbon black and H_2O) of the drop solution of the quinary MPEI $Pt(Fe_{0.7}Co_{0.1}Ni_{0.1}Cu_{0.1})$ and quinary HEA $PtFe_{0.7}Co_{0.1}Ni_{0.1}Cu_{0.1}$ based on drop solution calorimetry in molten sodium molybdate at 700 ℃ (see Methods for more details).

	Reaction	***ΔH* (kJ/mol)**
1	$x\ Pt(Fe_{0.7}Co_{0.1}Ni_{0.1}Cu_{0.1})@(1\text{-}x)C^{*}\ y\ H_2O^{\ddagger}_{(s,\ 25\,^{\circ}C)} + (1\text{-}x)\ O_{2\ (g,\ 700\,^{\circ}C)} \rightarrow x_1$(dissolved metals) $^{\dagger} + (1\text{-}x)\ CO_{2\ (g,\ 700\,^{\circ}C)} + y\ H_2O_{(g,\ 700\ ^{\circ}C)}$	$\Delta H_1 = \Delta H_{ds}$
2	$C_{(s,\ 25\,^{\circ}C)} + O_{2(g,\ 700\,^{\circ}C)} \rightarrow CO_{2(g,\ 700\,^{\circ}C)}$	$\Delta H_2 = -386.37^{a} \pm 1.12^{b}\ (3)^{c}$
3	$H_2O_{(l,\ 25\ ^{\circ}C)} \rightarrow H_2O_{(g,\ 700\ ^{\circ}C)}$	$\Delta H_3 = 69.0$
4	$H_2O_{(s,\ 25\ ^{\circ}C)} \rightarrow H_2O_{(l,\ 25\ ^{\circ}C)}$	$\Delta H_4 = 44.0$
Corrected drop enthalpy of dissolution of alloys (ΔH_{ds}'):		
$Pt(Fe_{0.7}Co_{0.1}Ni_{0.1}Cu_{0.1})_{(s,\ 25\,^{\circ}C)} \rightarrow$(dissolved metals)		
$\boldsymbol{\Delta H_{ds}' = [\Delta H_1 - (1 - x)\cdot\Delta H_2 - y\ (\Delta H_3 + \Delta H_4)]\ /\ x}$		

[a]averaged value, [b]two standard deviations of the average value, [c]number of measurements. [*]*x* values for the quinary MPEI and HEA are 0.02127 and 0.01984, respectively. [‡]H_2O is assumed to be adsorbed to the surface. The enthalpy of desorption (ΔH_4) is represented by equation 4. *y* values for ordered and disordered alloys are 0.008553 and 0.02672 respectively.

[†]The (dissolved metals) are $PtO_{2(sln,\ 700\,^{\circ}C)} + 0.7\ FeO_{2(sln,\ 700\,^{\circ}C)} + 0.1\ CoO_{(sln,\ 700\,^{\circ}C)} + 0.1\ NiO_{(sln,\ 700\,^{\circ}C)} + 0.1\ CuO_{(sln,\ 700\,^{\circ}C)}$.

Table S7. Enthalpies (ΔH_{ds}) and corrected enthalpies (ΔH_{ds}') of the drop solutions of the quinary (MPEI and HEA) and octonary (MPEI and HEA) nanoparticles.

Sample	ΔH_{ds} (kJ/mol)	ΔH_{ds}'(kJ/mol)
$Pt(Fe_{0.7}Co_{0.1}Ni_{0.1}Cu_{0.1})$ MPEI	-388.44 ± 1.97 (3)	-536.97 ± 44.86
$Pt(Fe_{0.7}Co_{0.1}Ni_{0.1}Cu_{0.1})$ HEA	-370.55 ± 2.40 (4)	-556.66 ± 41.27
$(Pt_{0.8}Pd_{0.1}Au_{0.1})_1(Fe_{0.6}Co_{0.1}Ni_{0.1}Cu_{0.1}Sn_{0.1})_1$ MPEI	-385.00 ± 1.75 (5)	-520.86 ± 96.39
$(Pt_{0.8}Pd_{0.1}Au_{0.1})_1(Fe_{0.6}Co_{0.1}Ni_{0.1}Cu_{0.1}Sn_{0.1})_1$ HEA	-376.31 ± 2.20 (4)	-552.12 ± 122.83

The enthalpy of transformation of quinary $Pt(Fe_{0.7}Co_{0.1}Ni_{0.1}Cu_{0.1})$ HEA → quinary MPEI is $\Delta H_{trans} = \Delta H_{ds}$'(MPEI) - ΔH_{ds}'(HEA) = -19.69 ± 60.96 kJ mol^{-1} (or -0.20 ± 0.63 eV per $Pt(Fe_{0.7}Co_{0.1}Ni_{0.1}Cu_{0.1})$ formula).

The enthalpy of transformation of octonary $(Pt_{0.8}Pd_{0.1}Au_{0.1})(Fe_{0.6}Co_{0.1}Ni_{0.1}Cu_{0.1}Sn_{0.1})$ HEA → octonary MPEI is $\Delta H_{trans} = \Delta H_{ds}$'(MPEI) - ΔH_{ds}'(HEA) = -31.3 ± 156.1 kJ/mol (or -0.32 ± 1.61 eV per $(Pt_{0.8}Pd_{0.1}Au_{0.1})(Fe_{0.6}Co_{0.1}Ni_{0.1}Cu_{0.1}Sn_{0.1})$ formula).

Table S8. Properties of the elemental precursor salts and metals.

Precursor salts	Decomposition temperature (K)	Chemical reduction potential (V)	Metal	Electronegativity
H_2PtCl_6	643	1.18	Pt	2.28
$PdCl_2$	948	0.95	Pd	2.20
$HAuCl_4$	473	1.50	Au	2.54
$FeCl_3$	579	-0.44	Fe	1.83
$CoCl_2$	1008	-0.28	Co	1.88
$NiCl_2$	~1073	-0.25	Ni	1.91
$CuCl_2$	703	0.34	Cu	1.90
$SnCl_2$	520	-0.14	Sn	1.96

Data from: https://ptable.com.

Video S1. MC modeling of the disorder-to-order transition process of quinary $PtFe_{0.7}Co_{0.1}Ni_{0.1}Cu_{0.1}$ (red, Pt atoms; green, Fe atoms; blue, Co atoms; white, Ni atoms; orange, Cu atoms).